Chapter 13

Bridging Cell and Tissue Behavior in Embryo Development

Alexandre J. Kabla, Guy B. Blanchard, Richard J. Adams and L. Mahadevan

Contents

The tissues of animal embryos utilize large-scale morphological transformations to bring about highly sophisticated body plans. In contrast with plant tissues, where differential growth and change in cell shapes are the main morphogenetic mechanisms, animal cells have in addition the ability to move with respect to their neighboring cells. Movement can be either active (cell motility) or passive, for instance as a response to an imposed strain. Despite the progress in genetics and molecular biology, our understanding of developmental biology still suffers a lack of experimental description and mechanistic interpretation of how individual cell behaviors lead to well-organized collective movements at the tissue scale. One of the outstanding issues concerns the role of mechanical forces, for instance as a driving force for passive morphological changes, or as involved in signaling pathways regulating active cell behavior. In this chapter we summarize a framework specifically designed to quantify the kinematics of embryo development. By analyzing clusters of neighboring cells, we developed a multiscale geometrical description that decomposes tissue strains into two contributions: one associated with changes in cell shapes and the other with cell–cell slippage or motility. The emphasis on cell shapes and cell–cell slippage provides, in particular, a fully continuous framework especially suitable to capture temporal and spatial heterogeneities regardless of discrete events such as neighbor exchanges. We also show here explicitly how the statistics of cell shape changes depend on a microscopic assumption regarding cell–cell slippage and propose a simple geometrical principle that can be used to deploy a consistent and robust approach.

13.1   Quantifying Embryo Morphogenesis

13.1.1   Morphogenesis of the Animal Embryo

Modern views of morphogenetic mechanisms have been built from a multidisciplinary approach to the study of the problem. Models must span from subcellular mechanisms of cellular mechanics, adhesion, and polarized cell behaviors to a mechanical understanding of substantial portions of the embryo and its environment. Morphogenetic mechanisms appear to encompass many classes of cell behavior, ranging from individual cell shape changes and movements to the collective reshaping of sheets of cells during such movements as invagination during sea urchin gastrulation [15], the convergence and extension of the vertebrate body axis [14], or the neurulation of the brain [8]. This class of collective reorganization is considered here, and key questions remain about identifying the patterns of passive and active cell behavior that shape the change in tissue morphology.

Our current understanding has closely followed the availability of tools, principally for microscopy, that have provided a means to address the dynamics of morphogenetic change in a noninvasive way. Variations among the trajectories of cells is the first indication of deformation of the tissue. For

instance, early studies by Jacobson on the neural plate of the newt pointed to a way of combining microscopic analyses and experimental manipulation to find a link between patterned regional variation in cell behavior—in this case, cell shape changes suggesting external mechanical forces responsible for the shaping of the neural plate [5].

While these early studies have been superseded, the basis of this approach is still recapitulated in current studies, including our own. To collect high-resolution and comprehensive 3-D data from which cell behavior and tissue morphogenesis can be measured has required the development of labeling and imaging methods capable of resolving cells in living embryos [17]. Software tools have been developed from which the trajectories and shapes of cells can be followed over time. Trajectories of cell centroids reveal the patterns of cell movements [7,16] but this is in itself difficult to interpret in terms of morphogenetic mechanisms until used to calculate tissue deformation [8,10] in the form of strain rates. Microscopic analysis of passive [13] and active tissue reshaping [20] has also provided evidence for cell movements or rearrangements underlying the morphogenesis of tissues.

13.1.2 Cell Intercalation and Rearrangements

Measures of cell area [5], cell neighbor number [22], and the change in cell neighbor topology [3] have been used to investigate the cellular mechanisms of morphogenesis. Interpretation of observations of cell rearrangements as passive or active events is highly dependent on additional biological or experimental insight into the problem. In recent years the power of molecular and genetic manipulation to investigate the relationship between cell behavior and morphogenesis has flourished, for instance in the role of planar cell polarity [23]. Deficiencies in cell behavior can be directly correlated with gross abnormalities of tissue morphogenesis [21]. However, to make full use of such methods, we require means of assaying the local morphogenetic characteristics of cells such as changes in their shapes and neighbor rearrangements. Independently, these measures give only their correlation but do not provide a direct link between events at the cell and tissue level. Linking them in a quantitative way is therefore necessary to explore causality and eventually identify underlying mechanisms.

Along that line, several novel approaches have been introduced to extract statistical and tensorial representations of cell behavior at a mesoscopic scale. Graner et al. [12] recently generalized tools primarily developed for foam mechanics into a generic framework for quantifying the strain and reorganization of cellular or granular materials based on the movement of cell centers and the evolution of their network of contacts. Their approach succeeds in relating material strains with the dynamics of neighbor exchanges, which represents one of the most visible characteristics of the long-term evolution of tissues.

On short time scales, however, neighbor exchange is a rare event and the local evolution of a piece of tissue is more appropriately described by

a combination of cell shape change and minute relative movements of cells that is referred to as cell–cell slippage. To account for this continuous reorganization, one can develop a kinematic approach by quantifying cell shape change rather than the dynamics of the cell contact network. In the following sections, we present in detail the construction of such a framework recently developed to analyze strains and cell behaviors during embryo morphogenesis [4]. It has been validated on a number of experimental situations in 2-D, such as the Drosophila germband extension [6], Drosophila dorsal closure [11], or zebrafish neural plate formation [19]. Another novelty in the framework, introduced in the final section, is the explicit link to a microscopic model of relative movement at the interface of neighboring cells. Although in practice reasonable choices can be made at that level, this opens the possibility of more subtle adjustments of the kinematic model in order to better account for the biological variety of cell behavior at the microscale.

13.2   Strain Measurements

The experimental measure of strain and strain rates during tissue morphogenesis requires us to monitor the motion of material points over time. In heterogeneous and composite materials, such as biological tissues, internal displacement fields can be highly complex and one needs to consider at which length scale and time scale a coarse-grained description is relevant. In the context of embryo morphogenesis, time scales are typically on the order of tens of minutes up to a few hours, and movements typically involve a large number of cells. Quantifying cytoskeletal and cytoplasmic movements inside cells is largely irrelevant as such flows occur on much shorter time scales and length scales. Although these might be important to understand the biological origin of collective movements, it is *a priori* enough, in order to characterize the deformation at the tissue scale, to average internal motion at the cell scale. This can be done, for instance, by tracking the cell center of mass (determined from the cell contour) or the locations of nuclei if the latter are labeled [8][1]. As discussed in Section 13.3, movements within the cell will also be considered, encompassed in a single tensorial quantity, the cell shape strain rate.

13.2.1   Introduction of a Mesoscopic Scale

From 3-D movies of developing embryos where cell membranes are fluorescently labeled [17], the contour of each cell is detected by image analysis and

---

[1]Only a marginal amount of extracellular matrix is present in embryo tissue at the early stages of development. One can therefore assume that cells are contiguous in the tissue and occupy all its volume.

the cell center of mass is computed [4]. Individual cells can be followed over time and their trajectories recorded, as well as their full shape, at any time. This can be implemented either for a 2-D epithelium or a 3-D tissue. A common situation corresponds to planar processes along curved surfaces, where the local strain is suitably accounted for by a 2-D description. In this chapter, the methods are illustrated using 2-D examples, although each step can be generalized in 3-D.

Kinematic quantities in the tissue are then defined and measured at a mesoscopic length scale at which we linearize the cell displacement field. We introduce a time scale δt and length scale n_c expressed as a number of cell diameters. The latter can either represent a topological distance (first neighbors, second neighbors, ...) or a physical distance. These two quantities are used to select a domain surrounding each cell at each time (Figure 13.1). More precisely, such a neighborhood, denoted by $N(i, t)$, is defined as the collection of cells located around the cell i, at time t, at a distance at most n_c; all these cells are followed during a time interval $[t - \delta t/2, t + \delta t/2]$. Although the connectivity of the cells can be used to define the neighborhood, it should be stressed that it is not a requirement; it only serves the purpose of conveniently defining a cohort of cells whose relative motion is tracked for a certain time.

13.2.2 Tissue Strain Rates

Defining absolute strains in embryos is often inconvenient due to the lack of a meaningful reference state and the complexity of handling the large finite strains that accumulate over time. Rather than using such quantities, we therefore focus on strain rates that can be easily mapped to reveal temporal and spatial patterns and conveniently integrated if necessary. In the following, we describe the generic approach used to estimate tissue strain rates from cell trajectories. Such methods are broadly used in hydrodynamics [18] and solid mechanics [9] to quantify intrinsic strains and strain rates, and have been successfully applied to geophysical measurements, in particular in the context of plate tectonics [1].

13.2.2.1 Velocity Gradient

By convention in this chapter the index i represents the identity of a cell. Vector symbols are underlined, and tensors are written in **bold** characters. The position of a cell over time, or trajectory, is denoted by $\underline{r}_i(t)$. The cell velocity in the reference frame of the microscope is $\underline{v}_i(t) = d\underline{r}_i/dt$, and is calculated by linearizing the cell displacement over a time interval $t \pm \delta t/2$. Within a neighborhood $N(i, t)$, one can define a number of averaged quantities. The position of the cohort is defined by:

$$\underline{R}_i(t) = \langle \underline{r}_{i'}(t) \rangle_{i' \in N(i,t)} \tag{13.1}$$
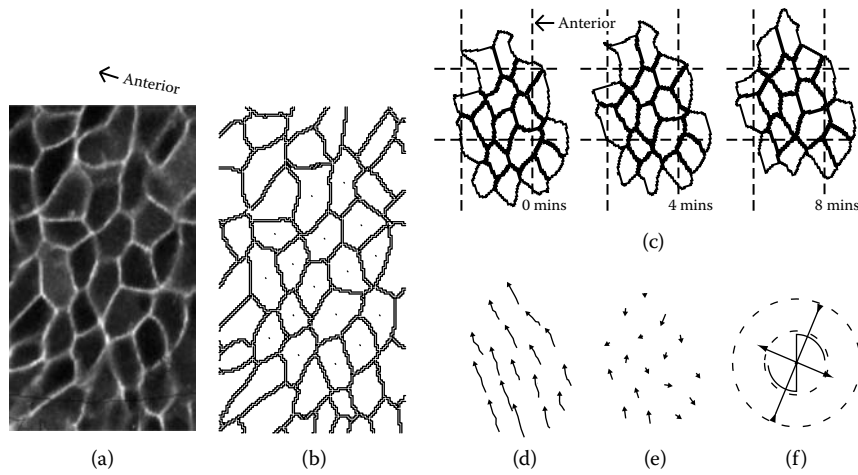
FIGURE 13.1 Example of tracking for a cell cohort in the zebrafish trunk. (a) Image of the first cellular layer flattened on a plane from a 3-D confocal stack. (b) Reconstructed cell membranes. (c) Evolution of a cell cohort, for the group radius corresponding to $n_c = 2$, and $\delta t = 8$ min. (d) Displacement field calculated from the above images. (e) Residual displacements once the mean velocity is subtracted. (f) Velocity gradient tensor $\mathbf{L_t}$ resulting from the linearization of the velocity field. The cross indicates the direction of eigenvectors of the symmetric part $\mathbf{D_t}$. The corresponding eigenvalues are coded in the length of the bars, with an arrow pointing outward for a positive eigenvalue (extension) or inward for a negative eigenvalue (convergence). The scythe motif represents the spin tensor $\mathbf{W_t}$, with a diameter in proportion to the magnitude of the antisymmetrical element. The radii of the dashed circles correspond to 0.8% and 1.6% per minute. (Data from [4].)

The average velocity of the cohort is:

$$\underline{V_i}(t) = \langle \underline{v_{i'}} \rangle_{i' \in N(i,t)} \tag{13.2}$$

The velocity field is then linearized within the neighborhood to calculate the velocity gradient tensor $\mathbf{L_t}$:

$$\underline{v_{i'}}(t) = \underline{V_i}(t) + \mathbf{L_t}\left(\underline{r_{i'}}(t) - \underline{R_i}(t)\right) + \underline{\delta v_{i'}} \tag{13.3}$$

The tensor $\mathbf{L_t}$ is, for instance, obtained from a least-squares fit of the experimental data. The residuals $\delta \underline{v_{i'}}$ can be used to assess the fit quality. The variation of the residuals with the neighborhood size n_c and integration time δt is in itself an interesting quantity that informs about the sources of the deviation, such as spatial heterogeneities, uniform noise in the position, etc. Nonaffinity in the displacement field is discussed later in this chapter.

13.2.2.2 Stretch and Rotation Rates

As strain rates intrinsically characterize infinitesimal strain increments, they can be appropriately decomposed into a sum of a stretch rate tensor $\mathbf{D_t}$ and a spin tensor $\mathbf{W_t}$, that is, a tensor accounting for the rate of rotation of the cohort domain. The tissue stretch rate tensor is defined as:

$$\mathbf{D_t} = \left(\mathbf{L_t} + \mathbf{L_t}^T\right)/2 \tag{13.4}$$

It is a symmetric tensor; its eigenvectors indicate the main axes of deformation, while the corresponding eigenvalues indicate the rate of elongation along these axes. The tissue spin tensor corresponds to the antisymmetrical part of the velocity gradient tensor:

$$\mathbf{W_t} = \left(\mathbf{L_t} - \mathbf{L_t}^T\right)/2 \tag{13.5}$$

13.2.3 Applications of Velocity Gradient Strain Tensor in Biology

The measurement of the velocity gradient tensor field has been applied to diverse embryological tissues, containing hundreds or thousands of cells, and for periods up to 3 hours [6,11,19]. For example, the fruit-fly germband converges to the ventral side of the embryo as it extends in the anterior–posterior axis in movements analogous to the convergence and extension of the vertebrate trunk. Analysis revealed that there was a gradient of increasing extension to the posterior, and a gradient of increasing convergence toward the ventral midline [6]. The latter gradient was correlated with tissue rotation in the flanking regions both anterior and posterior. The total accumulated strain of the tissue was comparable to published "shoelace" methods, and the time evolution of the process was found to be biphasic with a fast early phase followed by a slower phase. One direct advantage of mapping these quantities is to allow comparison between individuals to estimate inter-individual variability. The morphogenesis of the wild-type flies was then compared to various mutant fly strains whose morphogenesis is known to be abnormal during the convergence and extension process.

13.3 Cell Shapes and Intercalation

As mentioned in Section 13.1, changes in tissue morphology are accounted for at the cell scale by two main classes of evolution: cells can change shape and cells can rearrange (i.e., move relative to their closest neighbors). Both have a direct geometrical signature, and a proper kinematic description of
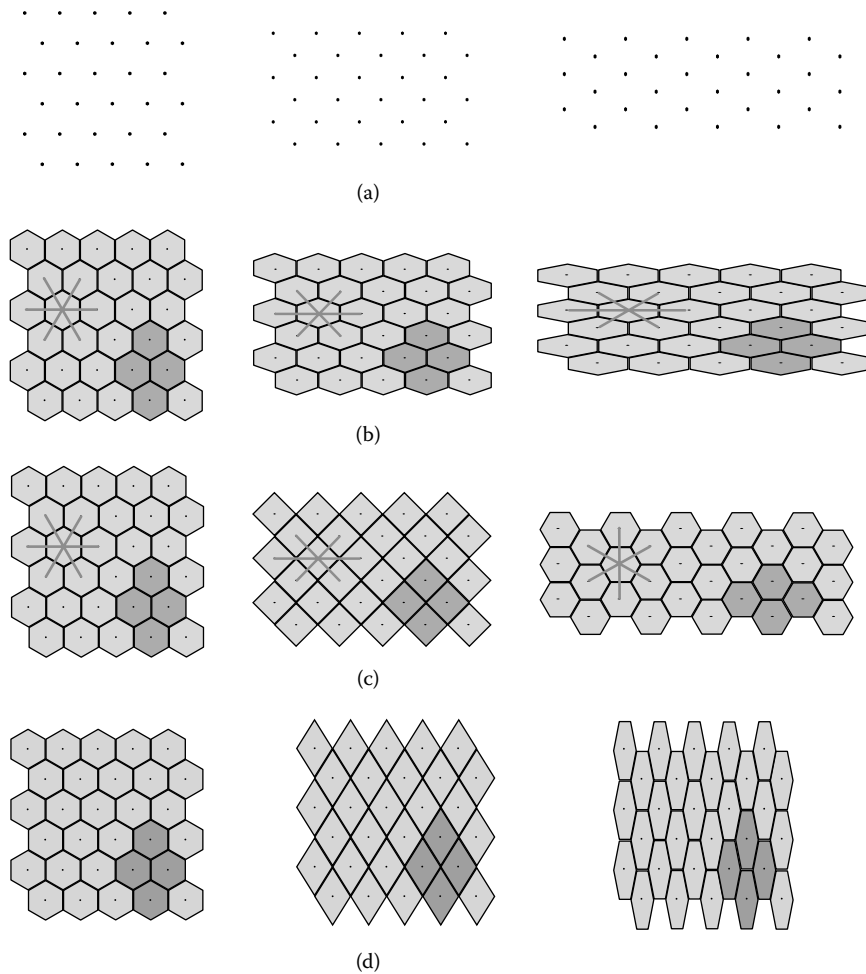
(a)

(b)

(c)

(d)

FIGURE 13.2 Schematic representation of the deformation of a piece of tissue; time increases from left to right. (a) Evolution of the cell centers, from which we can extract the tissue strain tensor. (b) and (c) Two opposite modes of shape deformations consistent with the tissue strain field shown in (a). The evolution of a ring of first neighbors is highlighted by line segments. (d) Shows another example where there is no tissue deformation, only a transfer between shape deformation and intercalation.

tissue morphogenesis must account for this. First, it should be highlighted that such information cannot be extracted from the motion of cell centers only. Figure 13.2 illustrates, for a uniform stretching of a regular hexagonal lattice, two different types of cellular dynamics that are consistent with the same overall tissue strain. In the first case (Figure 13.2(b)), the shape of

each cell experiences exactly the same strain as the piece of tissue. In the second situation (Figure 13.2(c)), although cell shapes slightly evolve over time, cells mostly compensate the tissue strain by moving past each other while remaining, on average, isotropic. This movement corresponds to a purely intercalating group of cells where all the deformation is associated with cell slippage, eventually leading to topological reorganizations in the sample, that is, neighbor exchanges. These two examples therefore demonstrate that cell shape evolves independently of the tissue strain according to their ability to intercalate. As shown in Figure 13.2(d), even if the tissue is not changing shape, there can be an interplay between cell shapes and cell slippage leading to a reorganization of the cells in the tissue. In addition to the motion of the centers, information must therefore be extracted from the dynamics of cell reorganization or cell shape evolution in order to discriminate between cell shape and intercalation-driven tissue reshaping processes.

The approach introduced by Graner et al. [12] addresses that issue; it uses the dynamics of the network of neighboring cells to track rearrangements in addition to the tissue strain. The authors build a number of statistical quantities from the distribution of links between first or second neighbors. Each cell rearrangement causes the network of first neighbors to evolve since links are gained where cells come closer, and lost in directions where cells move away. This allows the building of tensorial quantities to quantify both the tissue strain and the reorganization of the cell within the tissue. This method has a number of advantages, including a simple implementation in 2-D and 3-D, and a broad range of applications, in particular in the field of granular systems and colloidal suspensions where the contact network is more relevant than the individual shape of the particles. However, in the context of biological tissues, it starts capturing intercalation only when neighborhood relationships evolve. For instance, in the first two examples in Figures 13.2(b) and 13.2(c), such a method would see a difference between the shape- and intercalation-driven processes only after cells rearrange (second half) because until then, both the center of mass locations and contact networks are exactly identical in the two examples.

To capture the continuous nature of cell shapes and cell motility independently of cell rearrangements, we introduce in this section a general approach based on cell shape and its statistical evolution that allows us to quantify the respective contributions of both shape variations and intercalation movements to the total tissue extension previously studied. The definition of the intercalation tensor is then discussed in light of its microscopical interpretation.

13.3.1 Cell Shape Evolution

We aim to determine the strain tensor that accounts for the evolution in shape of the cells contained in a given neighborhood during the time interval δt, that is, that transforms the initial collection of cell shapes into a collection of shapes that is statistically equivalent to the final cell shapes, in terms of
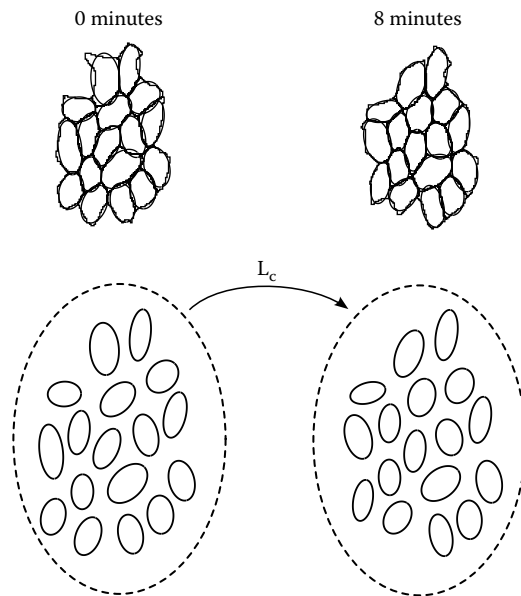
0 minutes   8 minutes

L_c

FIGURE 13.3   Illustration of the shape measurements. Top images show
the evolution of a cohort of cells. Elliptical fits of individual cells are overlayed.
The shape strain rate tensor is the transformation that, when applied to the
initial collection of ellipses, matches the distribution of shapes in the final
configuration.

orientation and elongation. Information concerning the relative placement of
cells (as used in the previous section) and their neighborhood relationship is
here irrelevant and discarded (see Figure 13.3).

Several approaches can be used to tackle this question. One is to consider,
for each cell individually, the strain rate that best matches the shape evolu-
tion. The question of identifying the strain that transforms one shape into
another has been extensively studied in image processing. Most registration
methods (optical flow, digital image correlation, etc.) estimate the physical
displacement of points in images and use it to deduce the local deforma-
tion. Unfortunately, such methods are not suitable for identifying the de-
formation of the cell shape because the movements of details of the mem-
brane geometry (which is the only morphological feature available here) is
locally non-affine and does not necessarily represent the average strain of
the cell bulk. This is illustrated on Figure 13.4 where a regular arrange-
ment of hexagon centers follows a simple shear deformation and cells ac-
commodate it mostly by sliding on each other. We used a full registration
method to estimate the strain tensor of individual shapes. The resulting ten-
sor captures primarily the movement of membranes, which results in typically
three solutions where the spin of the shape is either null or twice as big
as the rotation component of the tissue velocity gradient. It is difficult to
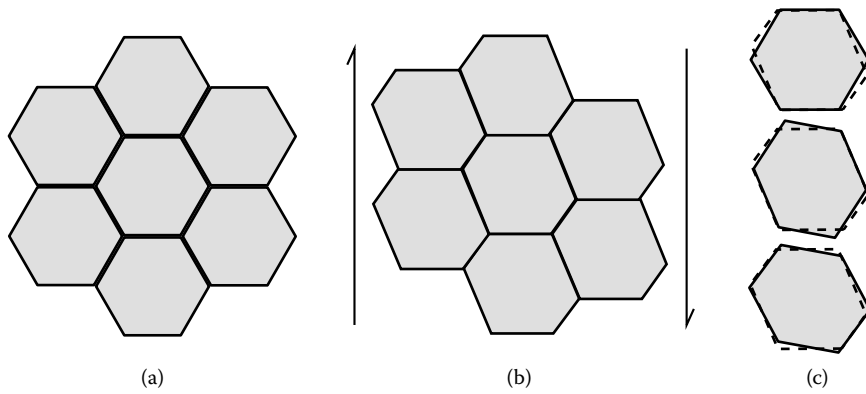
FIGURE 13.4 Typical issues arising with full registration methods applied to situations where non-affine shape deformations are present. (a) Regular hexagonal pattern. (b) Its evolution after a pure shear deformation. Shapes are recalculated in this example from the Voronoi tesselation of the cell centers. (c) Three local solutions for the shape strain typically obtained when trying to find the strain tensor that minimizes the nonoverlapping area. Dashed lines show the target shape displayed in (b), and the solid line, the calculated transformation of the initial hexagon in (a).

choose between these options, and there is no reason to believe *a priori* that the bulk of the cell tends to rotate on itself with respect to the tissue. This simple situation shows that, in general, registration methods on the membrane contour cannot be used to extract the cell shape strain. The only reliable information we can use at this stage corresponds to the global anisotropy of the cell shape, represented, for instance, by an elliptical fit to its shape. Another approach, introduced by Aubouy et al. [2] and not developed here, uses a (symmetric) texture tensor to characterize the average cell shape at the neighborhood scale. In all cases, we end up with an "elliptical" representation of the cell shapes, and we basically need to know what linear application transforms a given ellipse into another. Unfortunately, there is not a unique solution to the problem.

Let us define two elliptical shapes C_1 and C_2. Each of them is fully characterized by a pair of orthogonal vectors $(\underline{a}_1, \underline{b}_1)$ and $(\underline{a}_2, \underline{b}_2)$ representing, respectively, their minor and major axis directions and length (see Figure 13.5a). To transform C_1 into C_2, one can, for instance, first rotate C_1 until $\underline{a}_1$ is along $\underline{a}_2$, and then stretch the shape accordingly; or equivalently, first stretch the shape and then rotate it (Figure 13.5c). In both cases, points located along the main axis of C_1 end on the main axis of C_2. One could also directly search for a symmetric tensor that transforms C_1 into C_2 (Figure 13.5d). The eigenvectors of this tensor are not, in general, along the axis of either ellipse and, in contrast to the previous situation, the vectors $\underline{a}_1$ and $\underline{b}_1$ would not be mapped into the vectors $\underline{a}_2$ and $\underline{b}_2$. In fact, a continuum
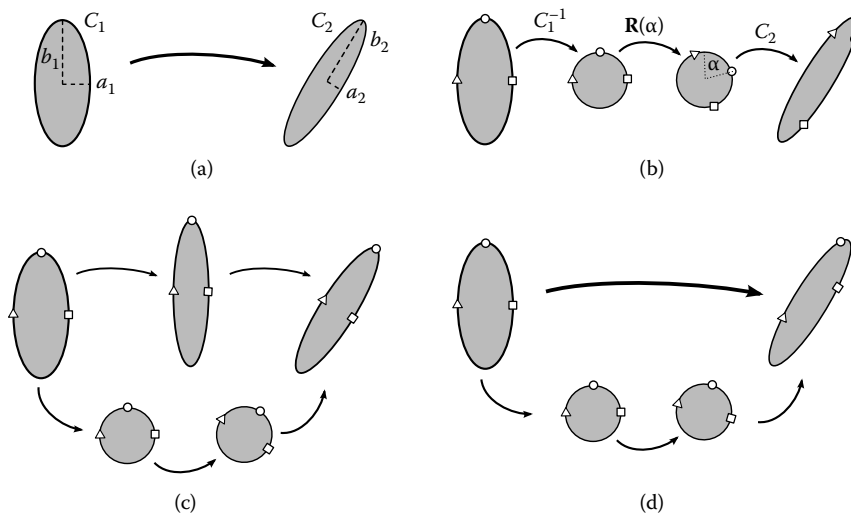
FIGURE 13.5 Family of deformations that transform one ellipse into another. (a) Description of the two ellipses C_1 and C_2. (b) Generic decomposition of the transformation into two stretches and an arbitrary rotation. Symbols indicate how a few specific points move with the deformation. (c) Example of a deformation that preserves the position of points with respect to the main axis of the ellipse. (d) Example of a deformation constrained to be symmetrical.

of solutions can easily be found. Let $\mathbf{C_1}$ and $\mathbf{C_2}$ be the (symmetric) stretch matrices that transform a circle of radius one onto, respectively, C_1 and C_2:

$$
\mathbf{C_1} = \left[\begin{array}{cc} a_1 & 0 \\ 0 & b_1 \end{array} \right], \mathbf{C_2} = \left[\begin{array}{cc} a_2 & 0 \\ 0 & b_2 \end{array} \right] \tag{13.6}
$$

expressed on the basis of unit vectors along the principal axis of C_1 and C_2, respectively. Let $\mathbf{R}(\alpha)$ be a rotation of angle α. For all values of α, the transformation $\mathbf{A}(\alpha) = \mathbf{C_2}\mathbf{R}(\alpha)\mathbf{C_1}^{-1}$ transforms C_1 into C_2 (see Figure 13.5b). Depending on the value of the angle α, the image of a given point along C_1 is going to move along C_2, as illustrated on Figure 13.5. This simple argument shows that building a strain tensor based on an elliptic representation of a shape is fundamentally undetermined.

A natural hypothesis to fully specify the shape deformation is to set the shape rotation component to match the tissue rotation, that is, so that the cells are not rotating with respect to the tissue. This ensures, in particular, that if a piece of tissue is uniformly rotated, the cell shape strain matches the tissue strain. In the case of a pure stretch of a tissue without intercalation, the shape deformation is also identical to the tissue strain, as expected. If we denote $\mathbf{L_c}$ as the cell shape strain rate, and use the same decomposition into
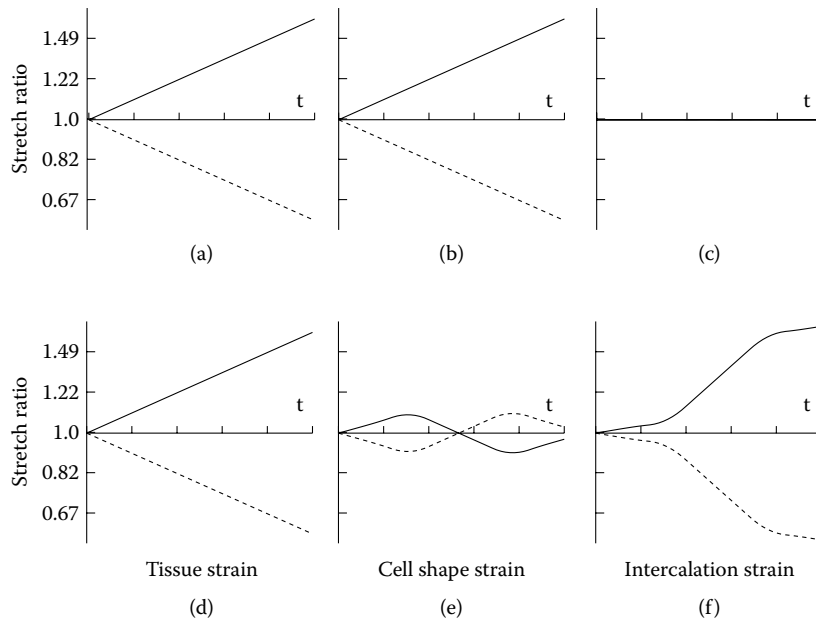
FIGURE 13.6 Evolution of the strains for the examples presented on Figures 13.2(b) (a to c) and 13.2(c) (d to f). The stretch ratio represents the ratio between the current tissue length and the initial length. Solid lines correspond to the direction of extension (horizontal), and dashed lines to the direction of convergence (vertical). From G.B. Blanchard, A.J. Kabla, N.L. Schultz, L.C. Butler, B. Sanson, N. Gornkiel, L. Mahadevan, and R.J. Adams (2009) Tissue tectonics: morphogenetic strain rates, cell shape change and intercalation. *Nature Methods*, in press. (With permission).

a symmetrical and anti-symmetrical part, we obtain:

$$\mathbf{L_c} = \mathbf{D_c} + \mathbf{W_c} \text{ with } \mathbf{W_c} = \mathbf{W_t} \tag{13.7}$$

A general method used to calculate the symmetrical component of the cell shape strain rate for a local domain is introduced in [4]. Figures 13.6(a) and b show the evolution of the total tissue strain for the hexagonal pattern described on Figure 13.2(b). In this example we find, as expected, that the cell shape follows precisely the tissue stretch. The same kind of plot is presented in Figures 13.6(d) and 13.6(e) for the intercalating tissue (Figure 13.2(c)). In that case, the shape strain slightly varies about zero, indicating indeed that cells do not deform on average.

As all the volume of the local group of cells is simply the sum of cell volumes (there is no free space between cells), the cell shape strain rate tensor must also account for any variation in tissue volume. This implies that the trace of $\mathbf{L_c}$ is identical with the trace of $\mathbf{L_t}$.

$$\text{Tr } \mathbf{L_t} = \text{Tr } \mathbf{L_c} \tag{13.8}$$

13.3.2   Tensorial Representation of Cell Intercalation

As suggested by the examples above (Figure 13.2), identical shape and tissue strain rates are a signature of nonintercalating tissues. On the other hand, the presence of collective slippage between cells leads to a mismatch between tissue strain rate and cell shape strain rate. More generally, the part of the tissue strain that is not accounted for by the shape evolution reflects collective movements of cells past each other. This suggests a very simple definition for a strain rate tensor $\mathbf{L_i}$ characterizing intercalation based on the shape change and tissue strain rate tensors, defined as:

$$\mathbf{L_t} = \mathbf{L_c} + \mathbf{L_i} \tag{13.9}$$

The physical meaning of this tensor is explored further in the next section. We calculated that quantity for the examples introduced on Figures 13.2(b) and 13.2(c), as plotted on the graphs in Figures 13.6(c) and 13.6(f) showing the evolution of the accumulated intercalation strain for both examples. As expected, there is no intercalation for the first case. More interestingly, there is a monotonic and continuous increase in the total intercalation for the second example. We can identify a few important properties of the intercalation rate tensor $\mathbf{L_i}$. First, the trace of $\mathbf{L_i}$ is zero, as all volume variations in the tissue are accounted for by the shapes. Second, assuming that the shape rotation is identical to the tissue rotation, $\mathbf{L_i}$ is symmetrical. It therefore has a diagonal form with two eigenvalues of opposite sign.

13.3.3   Handling Cell Division

While we monitor the evolution of a neighborhood, cell division might happen and rules regarding the handling of such events should be defined in the light of their influence on tissue deformation. If one considers the situation of a local neighborhood in which a cell division event occurs during the time of observation δt, the mere fact that a new membrane now splits a large cell into two smaller units does not influence directly the surrounding tissue (see Figure 13.7).What matters in practice is the change in cell shape before and after the division. As a consequence, to measure kinematic quantities that are relevant for a neighborhood, cells that divide during the time δt of the measurement are maintained artificially linked: the location and shape of the composite entity are obtained by merging the two cells. In practice, δt is small enough that cells remain in contact during the strain measurement.

13.3.4   Applications

The breakdown of the tissue strain rate tensor into cell shape and cell intercalation strain rate tensors allows us to map these two cell behaviors in space and over time in real tissues, just as can be done for the tissue strain rate tensor. Measured intercalation strain rates emerged as predominantly pure shear
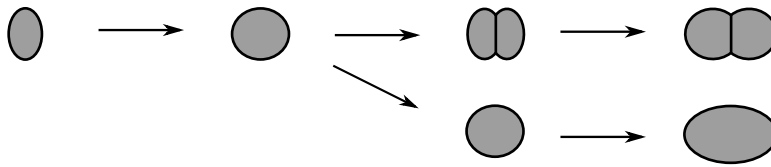
FIGURE 13.7 Illustration of the evolution of a cell elongating in a nonintercalating tissue. On the top path, one cell is followed through a sequence of change in shape, division event, and change in shape. On the bottom path, we represent a cell changing shape with a strain that is identical to the top situation with the daughter cells merged together. Both scenarios are expected to have the same effect on the surrounding tissue at a mesoscopic scale.

deformations, as predicted. In the fruit fly example [6] introduced in Section 13.2.3, the relative contributions of two cellular mechanisms were very revealing. Cell shape change and intercalation were equally strong during the early fast phase of germband extension, but cell shape change then reduced quite quickly, leaving only cell intercalation during the slow phase. Interestingly, in a mutant where the cell intercalation machinery was significantly compromised, the total tissue deformation was unaffected during the fast phase, but the relative contribution of the cellular mechanisms was different, with cell shape stretch significantly increased, compared to the wild-type flies, at the expense of cell intercalation. During the slow phase, cell shapes rounded up, suggesting that cell shape elongation was an elastic response to an external pull. Further insights have been gained into the formation of the zebrafish forebrain [8], convergence and extension in the zebrafish trunk [19], and the amnioserosa tissue of the fruit fly [11] using these methods.

13.4   Intercalation and Slippage

Intercalation is defined as the mismatch between the tissue strain rate and the cell shape strain rate. Its definition has been postulated from the fact that only cell intercalation can explain the difference between shape deformation and tissue strain. In this section we develop a microscopic interpretation of this tensor and show that it is intimately related to cell–cell slippage.

13.4.1   Cell–Cell Slippage

Our approach is based on the simultaneous quantification of movements within the cells (cell shape tensor) and at the cell cohort scale. The cell shape tensor is a very coarse description of material movement in the cell, which is known to be highly complex; it provides, however, the minimal description needed to compare cell and tissue strains. Figures 13.8(a) and 13.8(c) reuse the examples introduced on Figures 13.2(b) and 13.2(c) to illustrate the link between cell
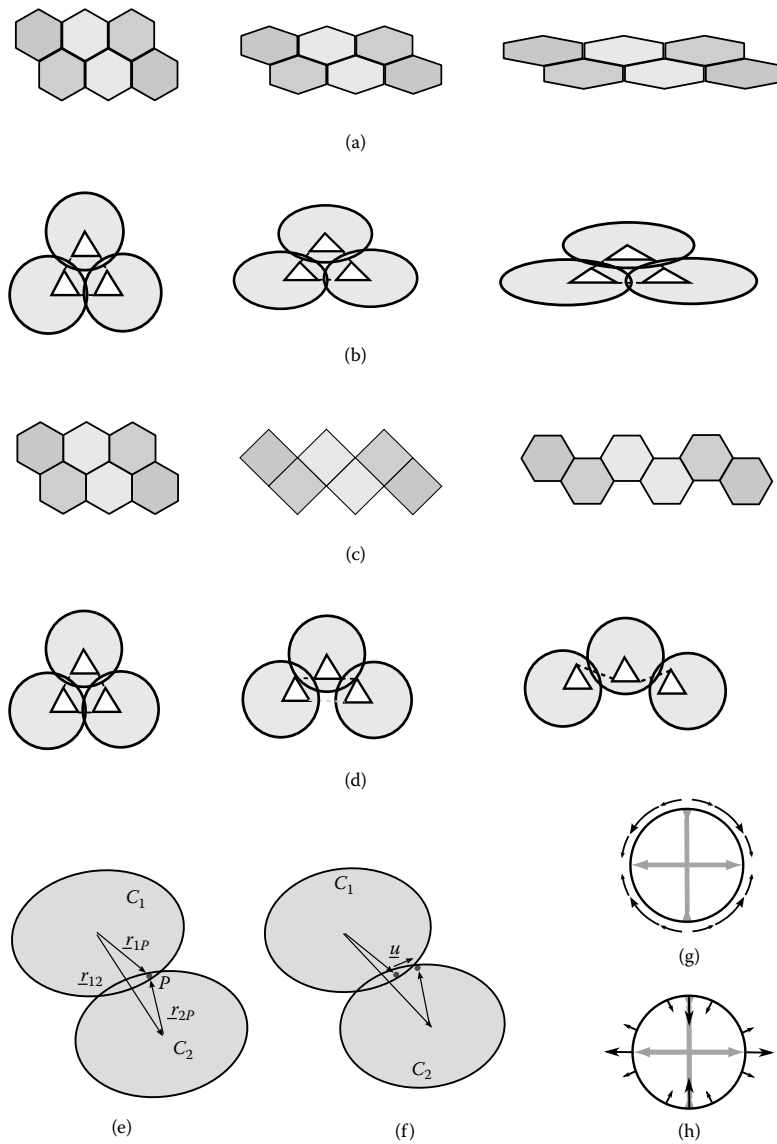
FIGURE 13.8   Illustration of the link between intercalation and slippage. (a) and (c) show a few cells extracted from Figures 13.2(b) (cell shape change) and 13.2(c) (intercalation), respectively. The ellipses in (b) and (d) represent the average shapes of cells in (a) and (c). White triangles within each ellipse are deformed accordingly to the cell shape strain tensor. (e) and (f) illustrate the construction of the slippage velocity (see text). (g) and (h) show the representation of the intercalation tensor in terms of slippage velocity. Vectors plotted along the circle correspond to the tangential (g) and normal (h) components of the slippage vector.

slippage and intercalation. The white triangles inside cells in Figures 13.8(b) and 13.8(d) evolve according to the cell shape strain rate $\mathbf{L_c}$ and allow us to visualize the strain within each cell. The shifts appearing among the three facing triangles during intercalation highlight, at the microscopic scale, the consequences of a mismatch of tissue and cell shape strain rates: in intercalating tissues, slippage occurs between neighboring cells, meaning that a domain about the cell interface necessarily experiences a local strain that does not correspond to the cell shape strain. Because we decided to ignore the complexity of the movements within cells, we represent here this complex flow near the cell membrane by a discontinuity at the cell interface, which can then be estimated geometrically.

We consider two neighboring cells C_1 and C_2. A point P is chosen along their interface. The velocity of P can be calculated in two different ways. Assuming it belongs to C_1, its velocity relative to the center of mass of C_1 is $\underline{u}_1 = \mathbf{L_c}\underline{r}_{1P}$. Assuming now it belongs to the cell C_2, its velocity would be $\underline{u}_2 = \mathbf{L_t}\underline{r}_{12} + \mathbf{L_c}\underline{r}_{2P}$. The discontinuity $\underline{u}$ at the interface can therefore be deduced:

$$\underline{u} = \underline{u}_2 - \underline{u}_1 = \mathbf{L_t}\underline{r}_{12} + \mathbf{L_c}\underline{r}_{2P} - \mathbf{L_c}\underline{r}_{1P} = (\mathbf{L_t} - \mathbf{L_c})\underline{r}_{12} = \mathbf{L_i}\underline{r}_{12} \qquad (13.10)$$

This construction demonstrates that the intercalation rate tensor is indeed a natural physical quantity for characterizing the movement of cells past each other. The velocity $\underline{u}$ has *a priori* components along and perpendicular to the cell membrane. In the case of the intercalating hexagons, the corresponding intercalation tensor as well as the tangential and normal components of the velocity $\underline{u}$ are shown in Figures 13.8(g) and 13.8(h).

The component u_s of $\underline{u}$ along the cell membrane is a direct measurement of slippage velocity. It has a maximum at an angle of about 45° of the main axis of the intercalation tensor (see Figure 13.5(g)). However, along the eigendirections of the latter, the slippage velocity vanishes, and most of the movement occurs normal to the interface. This component indicates the evolution of the ellipses overlap, corresponding qualitatively to the surface area of the cell–cell interfaces. Where $\underline{u}$ points inward, the contact area between the cells increases; where $\underline{u}$ points outward, the contact area decreases. Ultimately, this means that new neighbors are, respectively, gained or lost along these directions.

The description above sets the microscopic picture underlying the definition of the intercalation tensor introduced in the previous section. The framework provides us with three different scales: (1) the cell cohort, which is a mesoscopic scale to describe local tissue strain; (2) the single cell, for which we measure an internal strain rate; and finally (3) the cell–cell interface, along which slippage can be estimated.

13.4.2   Total Slippage

We assumed in the previous section that the rotation rate of cell shapes was the same as the tissue rotation rate. One argument for such a choice is that
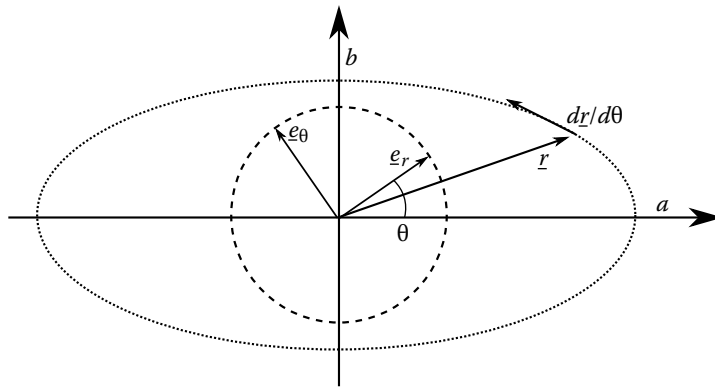
FIGURE 13.9 Geometrical symbols used in the text. The ellipse is parametrized by the angle θ: $\underline{r}(\theta) = (a\cos(\theta); b\sin(\theta))$.

it guaranties that cells of non-intercalating tissues do not rotate against each other. We need, however, to analyze further this choice as it is unclear how the same argument applies to fully or partially intercalating tissues.

We showed on Figure 13.5 that the choice of the shape rotation has a direct influence on the movements of points at the surface of an ellipse. Because these movements control, in part, cell slippage in the context of tissues, one can study how any particular assumption regarding cell rotation influences cell slippage at the microscale. A first step is to construct a measure of the total slippage required to transform the cell cohort and then explore ways to use such a physical quantity to build a self-consistent kinematic description.

The amount of cell–cell slippage S locally in the tissue can be quantified by integrating the squared slippage velocity along an elliptical contour C representing the average cell elongation in a neighborhood:

$$S = \int_C \left(\underline{u} \cdot \underline{e}_s\right)^2 ds \tag{13.11}$$

where s corresponds to the curvilinear abscissa along the ellipse. The ellipse contour C is parameterized by an angle θ so that $\underline{r}(\theta) = (a\cos(\theta); b\sin(\theta))$ (see Figure 13.9). Defining the matrix:

$$\mathbf{C} = \begin{bmatrix} a & 0 \\ 0 & b \end{bmatrix} \tag{13.12}$$

the position along the contour can be rewritten as $\underline{r}(\theta) = \mathbf{C}\underline{e}_r(\theta)$. The tangent to the ellipse is along $d\underline{r}/d\theta = \mathbf{C}\underline{e}_\theta$. The unit vector tangent to the ellipse is given by $\underline{e}_s = \mathbf{C}\underline{e}_\theta/(ds/d\theta)$. The total slippage can therefore be rewritten as:

$$S = \int_C \left(\mathbf{L_i}\mathbf{C}\underline{e}_r(\theta) \cdot \mathbf{C}\underline{e}_\theta\right)^2 \left(\frac{ds}{d\theta}\right)^{-1} d\theta \tag{13.13}$$

In Section 13.3.1, we characterized the family of deformations that transforms a particular ellipse into another. For each value of the angle α, we obtain a different shape strain tensor $\mathbf{A}(\alpha)$ that can be written for small strains as $\mathbf{A}(\alpha) = \mathbf{Id} + \mathbf{L_c}(\alpha)\delta t$. From this, the decomposition of the shape strain rate directly allows us to determine the tensors $\mathbf{D_c}(\alpha)$ and $\mathbf{W_c}(\alpha)$, the latter associated with the angular velocity $\omega_c(\alpha)$. For simplicity, we directly express the different tensors as a function of ω_c rather than α in the following.

For each value of ω_c, we therefore have a corresponding intercalation rate tensor $\mathbf{L_i}(\omega_c)$. Unless ω_c is identical to the tissue angular velocity, denoted by ω_t, $\mathbf{L_i}$ is not symmetrical, and has an antisymmetrical component corresponding to an angular velocity $\omega_i = \omega_t - \omega_c$. For a given cell elongation and a given tissue velocity gradient and shape evolution, we can now study how the total slippage S varies as a function of the shape angular velocity ω_c or equivalently ω_i. It remains true that $\mathrm{Tr}\,\mathbf{L_i} = 0$ for all ω_i, although all elements of the tensor change with ω_i, taking the general form below:

$$\mathbf{L_i}(\omega_i) = \begin{bmatrix} \beta(\omega_i) & \gamma(\omega_i) - \omega_i \\ \gamma(\omega_i) + \omega_i & -\beta(\omega_i) \end{bmatrix} \tag{13.14}$$

For small anisotropy of the cell shapes, the total slippage becomes (see Appendix at end of chapter for details):

$$S(\omega_i) = 2\pi(ab)^{3/2} \left(\omega_i^2 - \frac{1}{2}\left(\frac{a}{b} - 1\right)\omega_i\gamma + \frac{\beta^2 + \gamma^2}{2} \right) \tag{13.15}$$

The expression above shows that the total slippage $S(\omega_i)$ depends on both the cell shape aspect ratio and orientation with respect to the deformation. This leads to the identification of several cases of interest, as discussed below.

13.4.3 Typical Situations

13.4.3.1 Tissue Strain without Intercalation

If the tissue deforms with the velocity gradient $\mathbf{L_t}$, and if the same tensor $\mathbf{L_t}$ also deforms the cell shapes, this implies that $\mathbf{L_i}(\omega_i = 0) = \mathbf{0}$. Therefore, slippage is minimal for $\omega_i = 0$, as $S(\omega_i = 0)$ is strictly equal to zero. In the simple case of nonintercalating tissues, the shape strain rate that provides minimal slippage gives a meaningful output. Figure 13.10a shows the evolution of $S(\omega_i)$ in the context of a simple shear of both the tissue and the shape for a cell elongating along the shear direction ($a/b = 1.21$).

13.4.3.2 Tissue Intercalation along the Orientation of Cell Elongation

In the case where the tissue intercalates along one of the main orientations of the cell shape, $\mathbf{L_i}(0)$ is diagonal in the basis of the ellipse axes. It results in
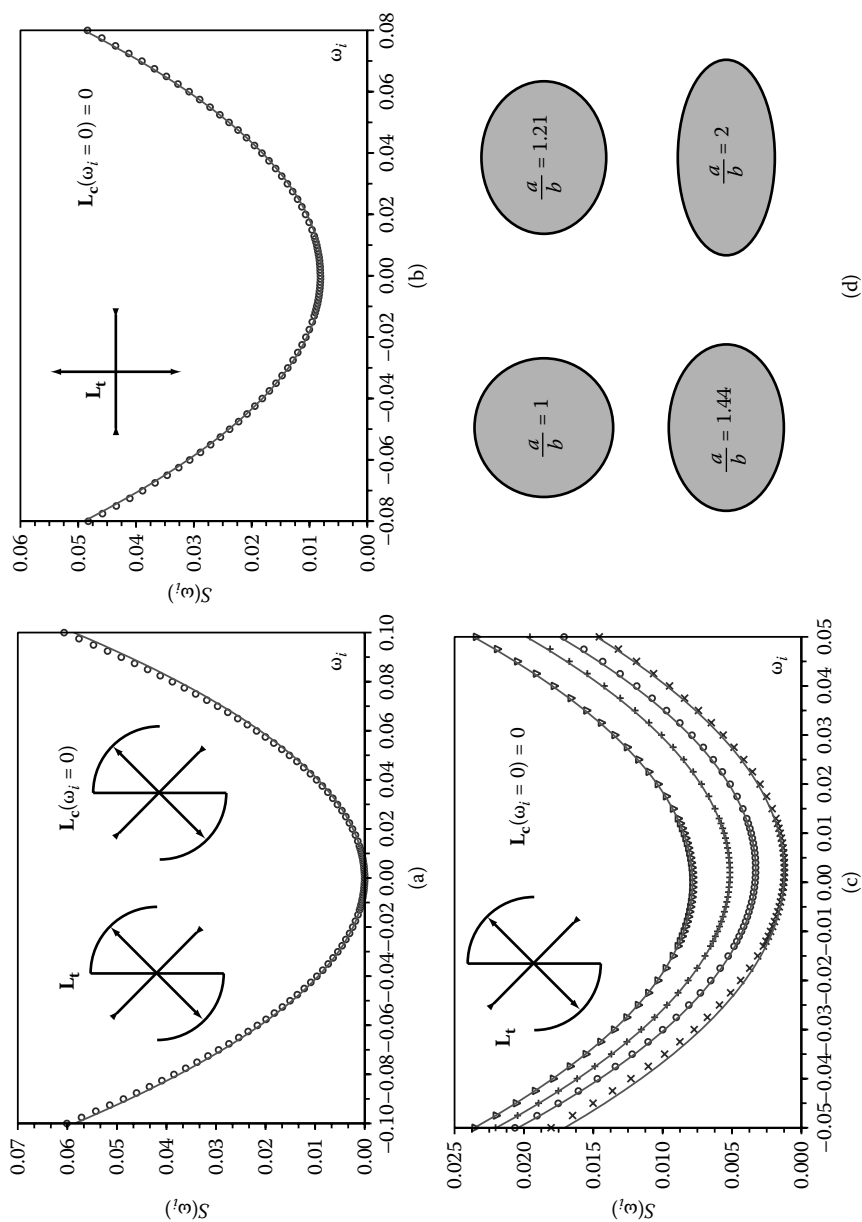
FIGURE 13.10 Total slippage calculated for a range of strain situations and cell shapes. Symbols correspond to the direct calculation of Equation (13.13). Solid lines show the small anisotropy approximation calculated from Equation (13.15). (a) Slippage for a simple shear deformation; $\mathbf{L_t} = \mathbf{L_c} = [0, 0.1; 0, 0]$, aspect ratio $a/b = 1.21$. (b) Pure intercalation along the cell principal axis of extension; $\mathbf{L_t} = [0.05, 0; 0, -0.05]$, $\mathbf{L_c} = 0$, $a/b = 2$. (c) Pure intercalation during a simple shear deformation, $\mathbf{L_t} = [0, 0.1; 0, 0]$, $\mathbf{L_c} = 0$, $a/b = 1, 1.21, 1.44$, and 2, respectively, from top to bottom. (d) Elliptical shapes for different values of the ratio a/b.

$\gamma(\omega_i = 0) = 0$. Moreover, by symmetry, $\gamma(\omega_i)$ is an odd function, implying that $\gamma(\omega_i) \sim \omega_i$. This means, in particular, that $S(\omega_i) = S(-\omega_i)$. Figure 13.10b displays the total slippage as a function of ω_i for such a situation, with highly elongated cells ($a/b = 2$). We observe indeed that the slippage is minimal when the shape rotates exactly with the tissue. This situation is quite frequent in reshaping tissues as the cell elongation is usually caused by the strain history itself, either as a passive adaptation or as an active contribution. In that situation, a symmetry argument is, in practice, enough to rule out any cell shape rotation other than the tissue rotation itself. It is also consistent with the minimal slippage idea.

13.4.3.3 Tissue Intercalation not along the Orientation of Cell Elongation

This corresponds to the most generic type of deformation. A common example is a simple shear deformation of a tissue with cells elongated along or normal to the shear direction. Such a case is addressed on Figure 13.10(c) for four values of the cell anisotropy. We observe that the shape spin that provides the smallest slippage is therefore different from the tissue spin. Consistent with Equation (13.15), this shift increases with the cell anisotropy. However, even for highly deformed cells ($a/b \geq 2$), the difference between tissue and shape rotation would be less than 10%.

In the three situations described above, our initial choice for the cell shape rotation rate seems justified *a posteriori* based on a minimal slippage argument. Assuming that the cells do not rotate in a reference frame attached to the tissue (i.e., $\omega_t = \omega_c$, $\omega_i = 0$) provides an excellent approximation, if not an exact answer. In many situations the result could come from symmetry arguments. However, in cases where the cell shape is not aligned with the eigenvectors of the intercalation strain rate tensor, there is no trivial answer and the robustness of the kinematic approach had to be verified. Although we provide here a workable and generic approach to quantify tissue morphogenesis, the kinematic description of cellular movements remains empirically linked with a microscopic assumption that sets the cell rotation and the amount of cell–cell slippage.

The main advantage of developing an approach based on slippage is to clearly highlight the microscopic origin and consequences of choices made at the tensorial level. Although it seems natural to penalize choices of rotation that induce unnecessary cell slippage, one should question how this penalty is practically determined, and in particular if slippage should be penalized the same way for all directions as we did above. The case of steady simple shear deformation is, for instance, a situation that remains to be explored. If cells move along layers, one can reasonably imagine that the slippage is mostly localized between layers, and not so much between cells of the same layer, as depicted on Figure 13.11. In such a situation, the kinematic description should
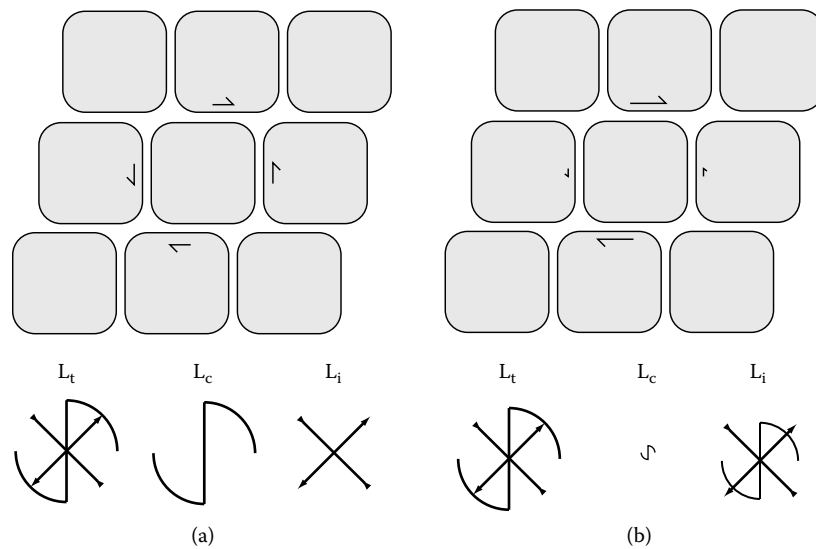
FIGURE 13.11   Two different shear situations: (a) Typical approach developed here, where cells rotate according to the tissue spin and slippage is shared among all neighbors; (b) Alternative situation in which slippage is more localized. To account for such a case, the minimal slippage argument must be adapted.

therefore account for the peculiarity of cell–cell interactions and be aware of the existence of planes of sliding arising either from anisotropic adhesion or active cell crawling. Allowing the intercalation tensor to have, in general, a rotational component then provides a natural way to express, within the same kinematic framework, that slippage inside cell layers is low compared to its value between layers.

13.4.4   Intercalation and Tissue Microstructure

Figure 13.8 provides a microscopic interpretation of the intercalation strain rate tensor. We first characterized in detail the slippage behavior of cells past each other, which mostly concerns cells contacting at about $45°$ to the eigenvectors of the intercalation tensors, where relative cell slippage is non-negligible (see Figure 13.8(g)). Cell movements along the direction of extension or convergence of the tissue are more subtle. Along these directions, slippage is low on average and the orientation of the relative velocity $\underline{u}$ defined in Equation (13.10) is mostly normal to the cell membrane, indicating that neighboring cells tend in practice to decrease or increase their contact area. However, these simple dynamics can only exist for a finite amount of time. The example of intercalating hexagons provides a good illustration of
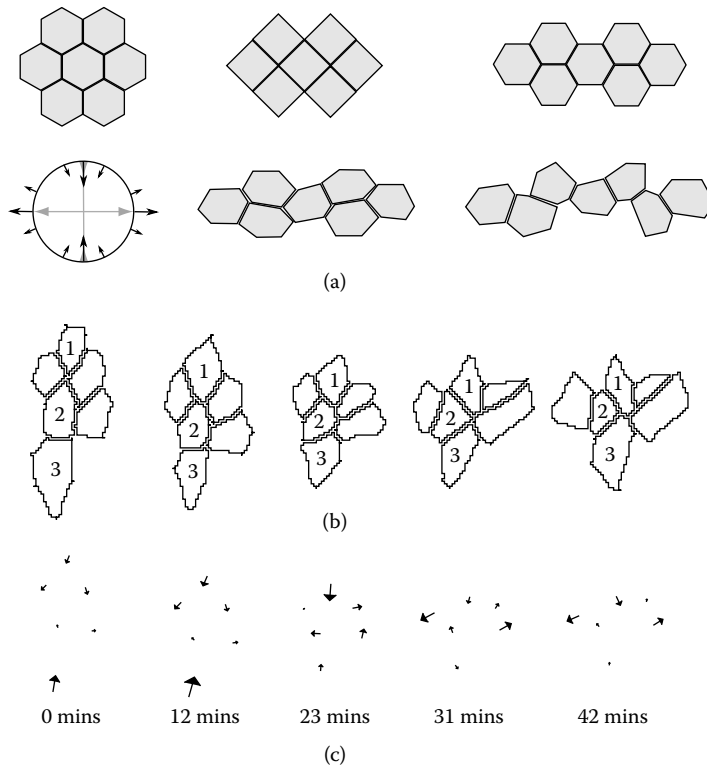
FIGURE 13.12 (a) Evolution of a purely intercalating tissue. During the first three steps, the hexagon network can deform in an affine way. Beyond that, non-affine displacement is required (images are only qualitative illustrations). (b) and (c) Details of the evolution of a few neighboring cells extracted from experimental data (zebrafish, [4]). As cells 1 and 2 come closer, the field is nearly affine. Once cells 1, 2, and 3 form a chain along the converging axis, highly non-affine displacements are required to satisfy the mean tissue and shape strains.

the process (Figure 13.12(a)), showing that even if it is well ordered, a purely intercalating tissue can reorganize in a homogeneous or affine manner only up to deformations on the order of 60%.

As cells move past each other, the detail of the distribution of membrane orientation evolves, creating, in particular, new contacts along the direction of convergence, and decreasing their number in the extension direction. Once cells come into contact along the direction of convergence, the affine displacement of cells becomes impossible and cells have to move in a non-affine way to accommodate the strain by intercalation. The last two steps of Figure 13.12(a) show a schematic of that process. Evidence of

such behavior can be readily found in experimental records. Figures 13.12(b) and 13.12(c) show the evolution over time of an intercalating cluster of cells. During the first 15 minutes, the displacement field is globally affine, and a pair of cells can be seen converging and forming a new interface. However, after 20 minutes, the cells 1, 2, and 3 form a chain that cannot intercalate further in an affine way without overlapping. From the resulting displacement fields, the non-affinity can be quantified by the value of $< \delta v_i^2 >$ at each time, $\underline{\delta v}_i$ being the residual velocity in Equation (13.3). For the five time steps shown on Figure 13.12(c), we measure $< \delta v_i^2 >=$ $0.10, 0.19, 0.87, 0.68, 0.52$, respectively, showing as expected a dramatic rise between 12 and 23 minutes.

Non-affine cell displacements cause significant heterogeneities in the velocity field (quantified above from the residuals). This also leads to variations in the cell shape strain rates within a neighborhood. The precise amount of slippage in a tissue has been therefore underestimated in our previous first-order approach, which neglected heterogeneities in the relative displacement field, in slippage, and in cell shapes. Non-affinity is probably not relevant at the tissue scale but, because it reflects the detailed structure and dynamics of the tissue and membrane orientation, it may highlight intrinsic mechanisms used by cells to produce or respond to macroscopic strains. In the case of living tissues, experimental studies must be carried out to quantify non-affinity and relate it to intrinsic material properties and in particular to its geometrical organization at the cell scale.

We developed a formalism here to quantify strains in reshaping tissues. In addition to strain rate measurements based on individual cell trajectories in the tissue, we introduced a quantification of cell shape changes and intercalation. The kinematic approach leads to a set of tensorial quantities defined for a local group of cells, approximating the local complexity by an affine description of the tissue deformation, and an elliptical representation of the cell shapes. Such a level of description represents a strong advantage to account for the global tissue morphogenesis; it allows us to define quantities that are continuous and easy to map with high resolution in space and time. We showed, in particular, that these quantities also reflect intrinsic cell behavior, such as shape change or slippage.

This framework introduces an explicit dependence on a microscopic assumption for cell–cell movements that sets the amount of rotation of the cell shapes. We propose to choose the rotation component so that cell–cell slippage is minimal; this corresponds in most practical cases to assuming that cells do not rotate in the tissue frame. However, this leads to nontrivial situations when, for instance, slippage occurs during a simple shear flow. Further development in quantifying morphogenetic movements will therefore be concerned with higher-order descriptions, accounting for the common and as yet unresolved situation of sheared layers and non-affine displacement fields.

13.5 Appendix: Total Slippage for Nearly Isotropic Cell Shapes

The measure S of the total slippage along the membrane of an ellipse can be calculated analytically if the intercalation rate tensor is known.

The geometrical notations used below are defined on Figure 13.9. The quantity S is calculated from Equations (13.13) and (13.14). We define the mean ellipse radius R and anisotropy λ by $R^2 = ab$ and $\lambda = a/R = R/b$. Equation (13.13) writes:

$$\tilde{S} = \frac{S}{R^3} = \oint_C \left(\mathbf{L_i} \tilde{\mathbf{C}} \underline{e}_r(\theta) \cdot \tilde{\mathbf{C}} \underline{e}_\theta \right)^2 \left(\frac{d\tilde{s}}{d\theta} \right)^{-1} d\theta \quad \text{with} \quad \tilde{\mathbf{C}} = \mathbf{C}/R = \begin{bmatrix} \lambda & 0 \\ 0 & 1/\lambda \end{bmatrix} \tag{13.16}$$

and $\tilde{s} = s/R$. This leads to:

$$\frac{d\tilde{s}}{d\theta} = \sqrt{\frac{1}{2} \left(\lambda^2 + \frac{1}{\lambda^2} - \left(\lambda^2 - \frac{1}{\lambda^2} \right) \cos(2\theta) \right)} \tag{13.17}$$

and

$$\mathbf{L_i} \tilde{\mathbf{C}} \underline{e}_r(\theta) \cdot \tilde{\mathbf{C}} \underline{e}_\theta = \frac{d\tilde{r}}{d\theta} \cdot \underline{\tilde{u}} = \gamma \cos(2\theta) - \frac{\beta}{2} \left(\lambda^2 + \frac{1}{\lambda^2} \right) \sin(2\theta) + \omega_i \tag{13.18}$$

Assuming small anisotropy for the cell shape, we define $\epsilon = \frac{1}{2}(\frac{a}{b} - 1)$ such as $\lambda \approx 1 + \epsilon$ and $\lambda^{-1} \approx 1 - \epsilon$. The two expressions above can be simplified into:

$$\frac{d\tilde{s}}{d\theta} = 1 - \epsilon \cos(2\theta) \tag{13.19}$$

and

$$\mathbf{L_i} \tilde{\mathbf{C}} \underline{e}_r(\theta) \cdot \tilde{\mathbf{C}} \underline{e}_\theta = \gamma \cos(2\theta) - \beta \sin(2\theta) + \omega_i \tag{13.20}$$

By substituting the slippage integral, we get:

$$\tilde{S} = \frac{S}{R^3} = \oint_C \left(\omega_i^2 - 2\epsilon \omega_i \gamma \cos^2(2\theta) + (\gamma \cos(2\theta) - \beta \sin(2\theta))^2 \right) d\theta \tag{13.21}$$

providing after integration a relationship corresponding to Equation (13.15):

$$\tilde{S} = \frac{S}{R^3} = 2\pi \left(\omega_i^2 - \epsilon \omega_i \gamma + \frac{\beta^2 + \gamma^2}{2} \right) \tag{13.22}$$

References

[1] R.W. Allmendinger, R. Relinger, and J. Loveless (2007). Strain and rotation rate from GPS in Tibet, Anatolia, and the Altiplano. *Tectonics* 26:TC3013.

[2] M. Aubouy, Y. Jiang, J.A. Glazier, and F. Graner (2003). A texture tensor to quantify deformations. *Granular Matter* 5:67–70.

[3] C. Bertet, L. Sulak, and T. Lecuit (2004). Myosin-dependent junction remodelling controls planar cell intercalation and axis elongation. *Nature* 429:667–671.

[4] G.B. Blanchard, A.J. Kabla, N.L. Schultz, L.C. Butler, B. Sanson, N. Gorfinkiel, L. Mahadevan, and R.J. Adams (2009). Tissue tectonics: morphogenetic strain rates, cell shape change and intercalation. *Nat. Meth.*, 6(6):458–464.

[5] M.B. Burnside and A.G. Jacobson (1968). Analysis of morphogenetic movements in the neural plate of the newt *Taricha torosa. Dev. Biol.* 18:537–552.

[6] L.C. Butler, G.B. Blanchard, A.J. Kabla, N. J. Lawrence, D.P. Welchman, L. Mahadevan, R.J. Adams, and B. Sanson (2009). Cell shape changes indicate a role for extrinsic tensile forces in *Drosophila* germband extension. *Nature Cell Biology*, 11(7):859–865.

[7] M.L. Concha and R.J. Adams (1998). Oriented cell divisions and cellular morphogenesis in the zebrafish gastrula and neurula: a time-lapse analysis. *Development* 125:963–994.

[8] S.J. England, G.B. Blanchard, L. Mahadevan, and R.J. Adams (2006). A dynamic fate map of the forebrain shows how vertebrate eyes form and explains two causes of cyclopia. *Development* 133:4613–4617.

[9] Y.C. Fung and P. Tong (2001). *Classical and Computational Solid Mechanics*, Singapore, World Scientific, Advanced Series in Engineering Science, Vol. 1.

[10] N.S. Glickman, C.B. Kimmel, M.A. Jones, and R.J. Adams (2003). Shaping the zebrafish notochord. *Development* 130:873–887.

[11] N. Gorfinkiel, G.B. Blanchard, R.J. Adams, and A. Martinez Arias (2009). Mechanical control of global cell behaviour during dorsal closure in *Drosophila. Development* 136:1889–1898.

[12] F. Graner, B. Dollet, C. Raufaste, and P. Marmottant (2008). Discrete rearranging disordered patterns. I. Robust statistical tools in two or three dimensions. *Eur. Phys. J. E.* 25:349–369.

[13] R. Keller and J.P. Trinkaus (1987). Rearrangement of enveloping layer cells without disruption of the epithelial permeability barrier as a factor in *Fundulus epiboly. Dev. Biol.* 120:12–24.

[14] R. Keller (2006). Mechanisms of elongation in embryogenesis. *Development* 133:2291–2302.

[15] T. Kominami and H. Takata (2004). Gastrulation in the sea urchin embryo: a model system for analyzing the morphogenesis of a monolayered epithelium. *Dev. Growth. Differ.* 46:309–326.

[16] T. Langenberg, T. Dracz, A.C. Oates, C. Heisenberg, and M. Brand (2006). Analysis and visualization of cell movement in the developing zebrafish brain. *Dev. Dynamics* 235:928–933.

[17] S.G. Megason and S.E. (2007). Fraser imaging in systems biology. *Cell* 130:784–795.

[18] L.M. Milne-Thomson (1996). *Theoretical Hydrodynamics*, 5th edition. New York, Dover Publications.

[19] N.L. Schultz, G.B. Blanchard, A.J. Kabla, L. Mahadevan, and R.J. Adams, Morphogenesis of the zebrafish neural plate, in preparation.

[20] J. Shih and R. Keller (1992). Cell motility driving mediolateral intercalation in explants of *Xenopus laevis. Development* 116:901–914.

[21] J.B. Wallingford, B.A. Rowning, K.M. Vogeli, U. Rothbcher, S.E. Fraser, and R.M. Harland (2000). Dishevelled controls cell polarity during *Xenopus* gastrulation. *Nature* 405:81–85.

[22] J. Zallen and R. Zallen (2004). Cell-pattern disordering during convergent extension in *Drosophila. J. Phys. Cond. Mat.* 16:S5073–S5080.

[23] J. Zallen (2007). Planar polarity and tissue morphogenesis. *Cell* 129:1051–1063.